
EXTENDING GENERALIZED DEBYE ANALYSIS TO LONG TIMESCALE MAGNETIC RELAXATION

A PREPRINT

Jeremy D. Hilgar

Department of Chemistry and Biochemistry
University of California, San Diego
La Jolla, California

Aaron K. Butts

Department of Chemistry and Biochemistry
University of California, San Diego
La Jolla, California

Jeffrey D. Rinehart*

Department of Chemistry and Biochemistry
University of California, San Diego
La Jolla, California
jrinehart@ucsd.edu

November 17, 2021

ABSTRACT

As the ability to generate magnetic anisotropy in molecular materials continues to hit new milestones, concerted effort has shifted towards understanding, and potentially controlling, the mechanisms of magnetic relaxation across a large time and temperature space. Slow magnetic relaxation in molecules is highly temperature-, field-, and environment-dependent with the relevant timescale easily traversing ten orders of magnitude for current single-molecule magnets (SMM). The prospect of synthetic control over the nature of (and transition probabilities between) magnetic states make unraveling the underlying mechanisms an important yet daunting challenge. Currently, instrumental considerations dictate that the characteristic relaxation time, τ , is determined by separate methods depending on the timescale of interest. Static and dynamic probe fields are used for long and short timescales, respectively. Each method captures a distinct, non-overlapping time range, and experimental differences lead to the possibility of fundamentally different meanings for τ being plotted and fitted globally as a function of temperature. Herein, we present a method to generate long-timescale waveforms with standard vibrating sample magnetometry (VSM) instrumentation, allowing extension of alternating current (AC) magnetic impedance measurements to SMMs and other superparamagnets with arbitrarily long relaxation time.

Keywords single-molecule magnetism · superparamagnetic relaxation · generalized Debye analysis · Cole-Cole Plot · lanthanide magnetism

Introduction

Single-molecule magnets (SMMs) are a class of zero-dimensional materials that utilize the spin-orbit interaction to generate an axially anisotropic angular momentum. Due to a preferred orientation along the anisotropy axis, the magnetization vector exhibits slow relaxation, as if it were a superparamagnet with a classic double well potential replaced by discrete quantum states.^{1,2} As a form of superparamagnetism, single-molecule magnetism cannot result in magnetic ordering. In recent years, however, the timescale of magnetic relaxation has extended drastically such that single magnetic ions are now shown to retain magnetization information for timescales exceeding 1 s in the liquid nitrogen temperature regime. At temperatures well below the superparamagnetic blocking temperature, T_B , these highly anisotropic systems can exhibit "frozen" dynamics due to their extremely long relaxation times, allowing the performance of typical permanent magnet characterization experiments, such as magnetization vs. field measurements

that display hysteretic behavior despite the lack of a permanent magnetic ground state. Magnetization vs. field scans contain information about the field dependence of quantum tunneling as well as the maximal magnetization and coercivity of the material. They do not, however, contain quantitative information about the number and time constants of the various relaxation processes contributing to the magnetic relaxation. This time-domain data is readily obtained as phase-dependent AC magnetic susceptibilities between approximately 0.001 and 1 s (AC relaxation), yet its collection becomes problematic at longer timescales. The standard method for determining long timescale relaxation time constants (DC relaxation) is to apply a large static magnetic field to magnetize a macroscopic amount of microcrystalline SMM material, remove the field as quickly as possible, and track the decay towards zero magnetization as a function of time. These data are a valuable source of information, yet have several drawbacks that can obscure the nature of the isolated molecular zero-field relaxation. First, there is a significant gap in measurement timescale between that captured by AC and DC relaxation (generally 1–10 min., depending on instrumentation capability). Second, commercial instrumentation is generally only capable of setting zero field within ± 30 Oe, leading to an inherent decay offset. In very sensitive systems, this small field offset can drastically alter the time constant or even completely change the dominant magnetic relaxation mechanism. Third, the scan from high field to zero field can instigate the transfer of energy between the (ostensibly isolated) molecules leading to propagating, multi-molecular relaxation processes. This last point especially contributes to multi- and stretched exponential dynamics that can obscure the molecular zero-field dynamics of interest for comparison to AC susceptibility relaxation data. Given the influx of new long-timescale SMMs and the need for analysis tools that leverage existing instrumentation, we sought to devise a method to extend the dynamic magnetization measurement methodology of AC susceptibility to longer timescales. Importantly, this design required compatibility with commonly-employed research magnetometers, similarity to the input signal characteristics of commonly used AC waveforms for probing magnetic relaxation, and extendability of the measurement to arbitrarily-long relaxation regimes. Herein we present a technique fitting these criteria whereby phase-dependent magnetic susceptibilities are extracted from standard vibrating sample magnetometer (VSM) measurements. To provide an initial demonstration of the method's efficacy, we examine the relaxation behavior of a variant of the SMM "erbocene" sandwich motif, $[\text{K}(\text{18-c-6})][\text{Er}(\text{hdcCOT})_2]$ (**1**, hdcCOT = hexahydrodicyclopentacyclooctatetraenide dianion, 18-c-6 = 18-crown-6) that has not been previously magnetically characterized.

Results and Discussion

Synthesis and solid-state structure

Preparation of compound **1** was carried out under air-free conditions using a procedure similar to that employed for its previously reported lithio analog, $[\text{Li}(\text{THF})(\text{DME})][\text{Er}(\text{hdcCOT})_2]$.³ Neutral hdcCOT was synthesized from 1,6-heptadiyne via a Ni^0 -catalyzed dimerization reaction⁴ and was subsequently reduced using potassium graphite (KC_8). The dipotassium salt of the alkyl-substituted COT dianion (K_2hdcCOT) reacted readily with a suspension of erbium trichloride in THF to give $\text{K}[\text{Er}(\text{hdcCOT})_2]$; δH (500 MHz; THF- d_8) –19.3 (br), –34.4 (br), –43.5 (br), –53.5 (br), –61.9 (br), –213.3 (br), –223.9 (br), –269.3 (br), and –343.3 (br) (Figures S1–S3). Removal of KCl and addition of 18-c-6 (to facilitate crystallization) yielded a solution which, when layered with pentane through vapor diffusion, deposited bright-yellow crystalline rods of **1**. X-ray analysis of these crystals showed that the solid-state structure of **1** includes an Er^{3+} ion in a homoleptic coordination environment with two hdcCOT²⁻ ligands coordinated in a 90° staggered conformation (Figure 1). Steric bulk is presumably responsible for the observed conformation about the metal center, however this bulk imparts no appreciable elongation of the average $\text{Er-hdcCOT}_{\text{centroid}}$ distance relative to an unsubstituted analog (CCDC⁵ Identifier YIWTUV^{6,7}). The potassium ion in **1** supports a κ^6 interaction to 18-c-6 as well as an η^4 interaction to one face of a hdcCOT²⁻ ring and the latter interaction lowers the hdcCOT–Er–hdcCOT sandwich angle from linearity to 178°.

Ab initio electronic structure

Previous studies on $[\text{Er}(\text{COT})_2]^{-6,7,8,9}$ and $[\text{Er}(\text{COT})]^{+10,11,12,13,14,15,16}$ motifs have demonstrated that a remarkably consistent single-ion anisotropy is generated at Er^{3+} when suitably equatorial coordination environments are selected. The efficacy by which the planar COT dianion in particular can stabilize prolate, high-moment m_J states on Er^{3+} has been well-rationalized by varying levels of theory and herein we modelled magnetic properties of **1** using complete active space, self-consistent field (CASSCF) methods (Figure S4). Decomposition of the calculated ground state spin-orbit wavefunctions into an m_J basis reveals that the lowered symmetry around the Er^{3+} center in **1** relative to unsubstituted $[\text{Er}(\text{COT})_2]^-$ species plays a negligible role toward wavefunction mixing and consequently the ground Kramers doublet is highly axial with 97.7% $m_J = \pm 15/2$ character. The first two excited doublets (94.7% $m_J = \pm 13/2$ and 93.1% $m_J = \pm 1/2$) are predicted to lie 169.2 and 211.3 cm^{-1} above the ground doublet. Ground to first and second excited Kramers doublet splittings have previously been calculated for $[\text{K}(\text{18-c-6})][\text{Er}(\text{COT})_2]^7$; interestingly, we observe no appreciable difference in calculated splittings between **1** and its unsubstituted analog and we anticipate alkyl-

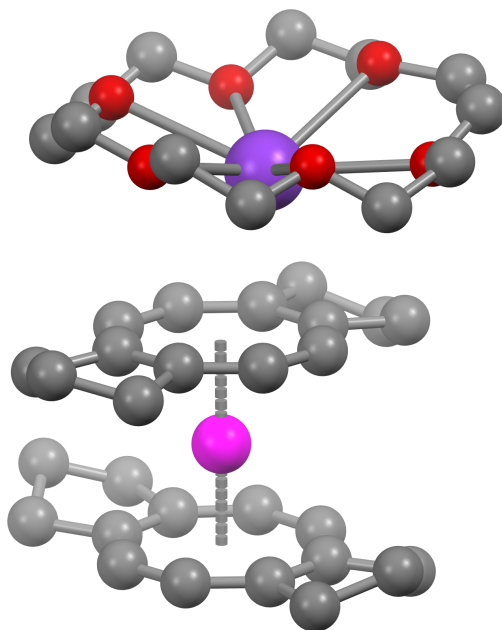


Figure 1: Solid-state structure of **1** with spheres representing Er (pink), K (purple), O (red), and C (gray). Hydrogen atoms and lattice THF molecules have been omitted for clarity.

substitutions on COT play a marginal role in affecting low-energy spin-orbit states on erbium. Transverse magnetic moment matrix elements connecting states within the $J = 15/2$ manifold have also been calculated. As discussed elsewhere,¹⁷ the square of these matrix elements are roughly proportional to transition rates between the states that they connect and the effective barrier of magnetic reversal (U_{eff}) in the high-temperature limit can be approximated as the shortest path between ground states with non-negligible matrix elements. Calculated matrix elements between the ground doublet and first excited doublet are small (3.3×10^{-6} and $5.1 \times 10^{-4} \mu_B$, respectively) which indicate that QTM between these states should be suppressed. Matrix elements connecting the second excited doublets ($m_J \sim \pm 1/2$) and cross-terms between the first and second excited doublets (e.g. $m_J \sim +13/2$ and $m_J \sim -1/2$) are larger (3.2 and $4.1 \times 10^{-2} \mu_B$, respectively) and likely relaxation pathways in the high temperature limit will involve thermally assisted quantum tunneling of the magnetization (QTM) or Orbach relaxation modes through the second excited Kramers doublet.

Magnetic characterization

Static magnetism

Zero-field cooled static magnetic susceptibilities for **1** were measured over 2–300 K with a 1000 Oe bias field and the data were plotted as the molar susceptibility times temperature product (χT) vs. temperature (Figure S5). At 300 K, $\chi T = 11.69 \text{ emu mol}^{-1} \text{ K}$, which is close to the expected value for an Er^{3+} ensemble with equal populations across the $J = 15/2$ spin-orbit manifold ($\chi T = 11.49 \text{ emu mol}^{-1} \text{ K}$). As T is lowered from 300 K, χT shows a small decline as this manifold becomes thermally depopulated. At 12 K, $\chi T = 11.24 \text{ emu mol}^{-1} \text{ K}$; below this temperature the data display a precipitous drop to $1.60 \text{ emu mol}^{-1} \text{ K}$ at 2 K. This drop is indicative of magnetic blocking on the timescale of the DC scan and thus isothermal magnetization measurements ($H_{max} = |7| \text{ T}$, 10 Oe sec^{-1} ramp rate) were collected to further probe for superparamagnetic behavior. At 2 K, the magnetization saturates at $4.98 \mu_B \text{ mol}^{-1}$ when the field is swept above 3.5 T. Consistent with the ZFC results, hysteretic behavior is observed when the field is swept back from 7 T. Near 0 T, the magnetization drops abruptly to $1.25 \mu_B \text{ mol}^{-1}$ and the application of negative fields yields a coercivity $H_C = 1.1 \text{ T}$ on this timescale. Zero-field magnetization loss and waist-restricted hysteresis are commonly observed in SMMs when transverse crystal field (CF) components enable fast relaxation via QTM between ground states.¹⁸ Symmetry optimization strategies can be employed to mitigate this effect and in the case of $[\text{Er}(\text{COT})_2]^-$ species the pseudo- C_∞ axis minimizes transverse CF components to yield a ground doublet within which QTM is largely quenched. The striking zero-field magnetization loss in **1** mimics well the behavior observed in $[\text{K}(18\text{-c-6})][\text{Er}(\text{COT})_2]$ which, through a magnetic dilution study with yttrium, was shown to be facilitated by a bulk magnetic avalanche effect.⁶

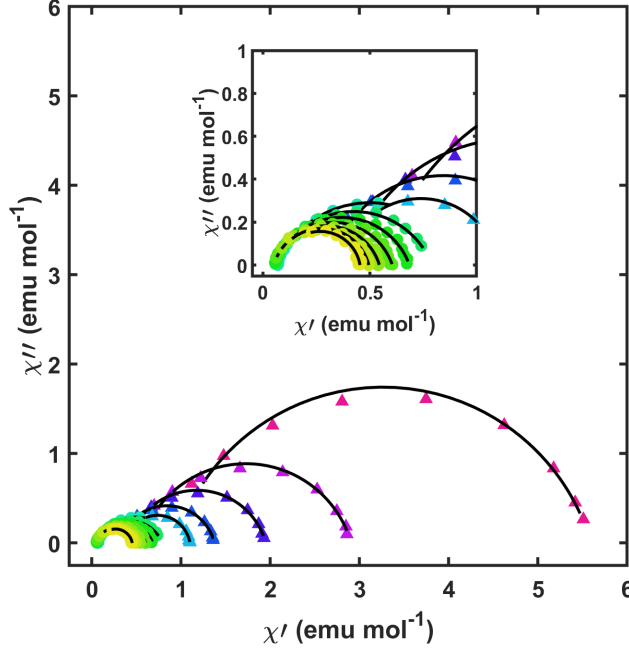


Figure 2: Cole-Cole plot of **1** between 2–24 K. Colored points are susceptibilities measured via standard AC measurements (circles) and extracted from Fourier analysis of VSM data (triangles). Black lines represent fits a generalized Debye model (Equations 1 & 2).

Dynamic magnetism

Consistent with SMM behavior, the AC susceptibility phase-shift of **1** shows a clear dependence on drive-field frequency below 24 K and short time-scale relaxation times were extracted from these data by simultaneously fitting the in-phase (χ') and out-of-phase (χ'') signals ($H_{DC} = 0$ Oe, $f = 0.1$ –1000 Hz, $T = 12$ –24 K) to a generalized Debye relaxation model (Figure 2, Equations 1 and 2).¹⁹

$$\chi'(\omega) = \chi_S + (\chi_T - \chi_S) \frac{1 + (\omega\tau)^{1-\alpha} \sin(\pi\alpha/2)}{1 + 2(\omega\tau)^{1-\alpha} \sin(\pi\alpha/2) + (\omega\tau)^{2-2\alpha}} \quad (1)$$

$$\chi''(\omega) = (\chi_T - \chi_S) \frac{(\omega\tau)^{1-\alpha} \cos(\pi\alpha/2)}{1 + 2(\omega\tau)^{1-\alpha} \sin(\pi\alpha/2) + (\omega\tau)^{2-2\alpha}} \quad (2)$$

Fitted eccentricities are low ($\alpha_{max} = 0.25(1)$) indicating a single relaxation time with a narrow distribution is associated with each temperature across the measured frequency range. A plot of $\ln(\tau)$ vs. $1/T$ (Figure 5) shows that an over-barrier Orbach relaxation mechanism is operant in this temperature range and least-squares fitting to an Arrhenius Law yielded an effective barrier height $U_{eff} = 147.7(7)$ cm⁻¹ ($\tau_0 = 3.1(1) \times 10^{-8}$ s). A previous analysis on [K(18-c-6)][Er(COT)₂] yielded an effective barrier $U_{eff} = 147$ cm⁻¹; this striking similarity further corroborates our *ab initio* results which suggested that the alkyl substitutions on the COT ring play a negligible role toward modifying the crystal field environment around Er³⁺.

Preliminary studies on relaxation dynamics longer than the MPMS3 AC timescale (< 0.1 Hz) were conducted between 2–10 K by measuring the zero-field DC relaxation profile of a sample previously in equilibrium with a 7 T field. Consistent with the presence of a small remnant field in the MPMS3 superconducting magnet, final moments are negative and their magnitudes range from 0.37–1.8% relative to the moment at $t = 0$ s. This residual field is typically on the order of 20–30 Oe and two approaches used to minimize it include oscillating the field to zero and resetting the magnet (see e.g. "MPMS Application Note 1014-208," Quantum Design, 2001). We note that neither approach is feasible during the DC relaxation experiment. Given that multiple distinct processes or a distribution of processes are typically responsible for SMM relaxation at a given temperature, several forms of exponential decay models are

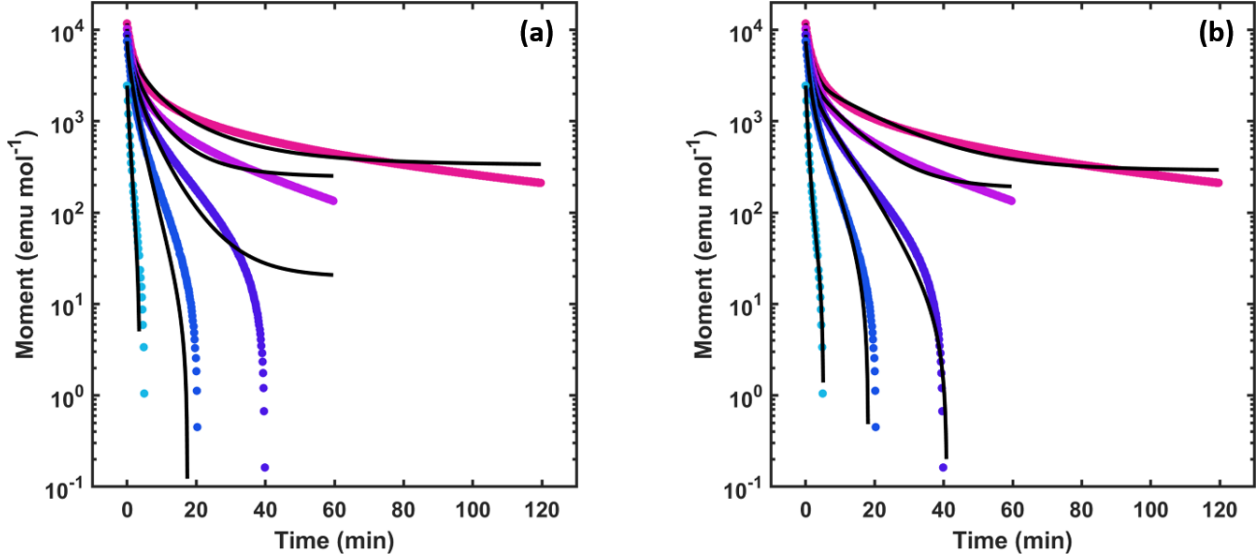


Figure 3: DC relaxation data of **1** between 2–10 K. Colored points are moments measured from near-zero-field DC scans. Black lines are fits to (a) stretched and (b) bi-exponential models.

routinely used to extract relaxation times in the long time-scale regime. Herein we fit DC relaxation data of **1** (Figure 3, Table 1) using a stretched exponential (Equation 3, $0 < \beta < 1$) and a bi-exponential model (Equation 4).

$$M(t) = M_f + (M_0 - M_f) \exp\left(\frac{-t}{\tau_{str}}\right)^\beta \quad (3)$$

$$M(t) = M_f + (M_0 - M_f) \left[A_{1,2} \exp\left(\frac{-t}{\tau_1}\right) + (1 - A_{1,2}) \exp\left(\frac{-t}{\tau_2}\right) \right] \quad (4)$$

Corroborating with the observation of multiple potential relaxation mechanisms in the magnetization data, we found that a simple exponential equation (Equation 3, $\beta = 1$) does not adequately model the relaxation behavior of **1** below 10 K. Disagreement between data and fits become more prominent as temperature is lowered and it is evident that the extracted relaxation time is biased toward the short time-scale. Agreement between the data and fit can be improved with the addition of a stretching parameter, β to the exponential. Similar to the α parameter of the generalized Debye equation, β accounts for a distribution about an average relaxation process. Incorporation of β results in the extraction of relaxation times with wide distributions at low T ($\beta_{2\text{K}} = 0.505(9)$). A similar quality fit was obtained when two exponential relaxation processes were used to model the data. Interestingly, this model reveals that relaxation of **1** can be rationalized by two processes operating on significantly different timescales (i.e. separated by an order of magnitude at 2 K) with the long relaxation time τ_1 and short relaxation time τ_2 bracketing the relaxation times obtained previously with a stretched exponential model. The presence of a small residual field (*vide supra*) during the DC relaxation measurement provides a potential explanation for the observed long timescale process. This field can lift Kramers degeneracy between bistable orientations of the ground state and concomitantly hinder QTM. The addition of further constants and weighting factors would undoubtedly improve the fit, yet the ambiguity of the existing parameters and their importance to the intrinsic zero-field molecular relaxation make further parameterization of dubious value.

VSM waveform analysis

Prompted by the desire for more quantitative information about long-timescale relaxation, we sought a method that could more faithfully model the zero-field relaxation dynamics of **1**. Ideally the method would be well-suited for extracting τ information from non-ensemble magnetic processes and would furthermore be capable of directly probing for the existence of multiple such relaxation processes. Naturally, Debye model fitting of complex AC magnetic susceptibilities fit these criteria well and is the standard when relaxation times fall within common magnet modulation coil limits ($\nu = 0.1$ –1500 Hz). An interesting question that follows from the preceding is whether complex susceptibilities can be reliably extracted from data collected from waveforms constructed in either DC or VSM scan modes. Although magnetic field controls have a limited linear sweep rate ($R_{H_{max}} = 1.6 \text{ Oe sec}^{-1}$ for the Quantum Design MPMS3 magnetometer), drive fields of arbitrarily low frequency can be generated if an appropriate waveform is selected. To

Table 1: Long time-scale relaxation times of **1** extracted from various models.

T (K)	Equations 1 & 2		Equation 3		Equation 4		
	τ_{VSM} (s)	α	τ_{str} (s)	β	τ_1 (s)	τ_2 (s)	$A_{1,2}$
2	54(4)	0.18(4)	145(3)	0.505(9)	1093(29)	87(1)	0.222(4)
4	43(3)	0.18(4)	119(3)	0.58(1)	621(18)	69(1)	0.252(6)
6	37(3)	0.17(4)	106(2)	0.62(1)	442(9)	61.8(8)	0.271(5)
8	33(2)	0.15(5)	81(1)	0.74(1)	241(5)	52.7(6)	0.271(7)
10	13.4(8)	0.10(3)	36.3(4)	0.88(1)	122(8)	30.6(4)	0.13(1)

Parentheses following fitted values represent 95% confidence intervals.

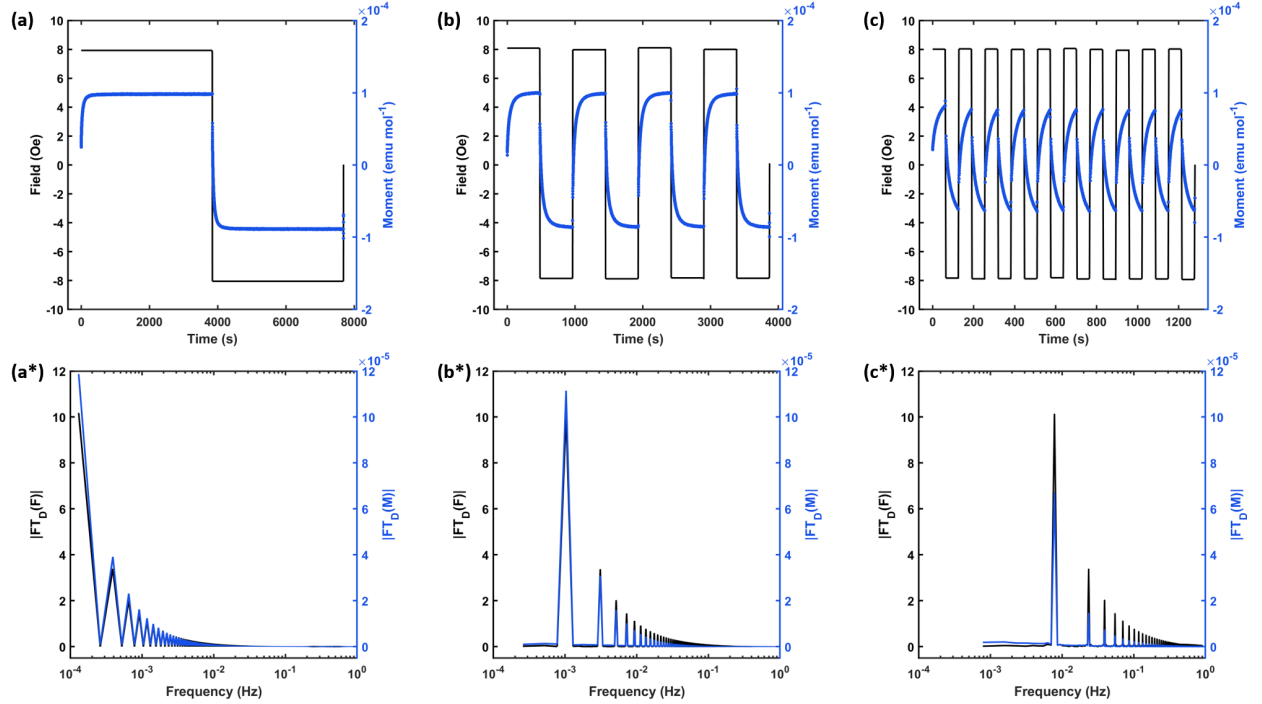


Figure 4: Representative raw VSM waveform data (top row) and discrete Fourier transform of VSM waveform data (bottom row) with period lengths 7688 s (a and a*), 968 s (b and b*), and 128 s (c and c*). Black lines are field values and purple lines are measured moments.

test whether phase information could be extracted from **1** outside the typical AC scan range, we developed a sequence which measures VSM moments generated by a square-wave magnetic drive field oscillating about 0 Oe ($H_{max} = 8$ Oe, $R_H = 30$ Oe sec⁻¹). Our initial studies on this approach yielded profiles of average moment significantly different from 0 emu mol⁻¹, indicating a persistent offset from zero bias field. A single magnet reset operation before data collection was sufficient to remove this residual field, allowing measurement of periodic moments with no appreciable offset (Figure 4a–c). To optimize sequence run times, magnetic field cycle counts were scaled with frequency (e.g. 20 cycles were measured at 0.0264 Hz and 1 cycle was measured at 0.00013 Hz). An example truncated MPMS3 sequence file can be found in Listing 1 in the SI. The discrete Fourier transform was applied to H vs. t and M vs. t data which yielded complex-valued frequency space representations. Plots of the absolute value of the transform vs. frequency revealed spectra with a primary peak at the fundamental drive field frequency followed by overtone peaks of diminishing intensity. We set $\chi = |FT_D(M_{max})|/|FT_D(F_{max})|$, where $|FT_D(M_{max})|$ and $|FT_D(F_{max})|$ are absolute values at the fundamental frequency of the complex moment and field spectra, respectively. The in-phase (χ') and out-of-phase (χ'') components of the magnetic susceptibility were then calculated as $\chi' = \chi \cos(\phi)$ and $\chi'' = \chi \sin(\phi)$, with ϕ being the phase angle between the field and moment spectra at the fundamental frequency. Using this method, complex susceptibilities were extracted from VSM moment waveforms of **1** collected at temperatures between 2–10 K using square-wave drive fields with periods between 38–7690 s.

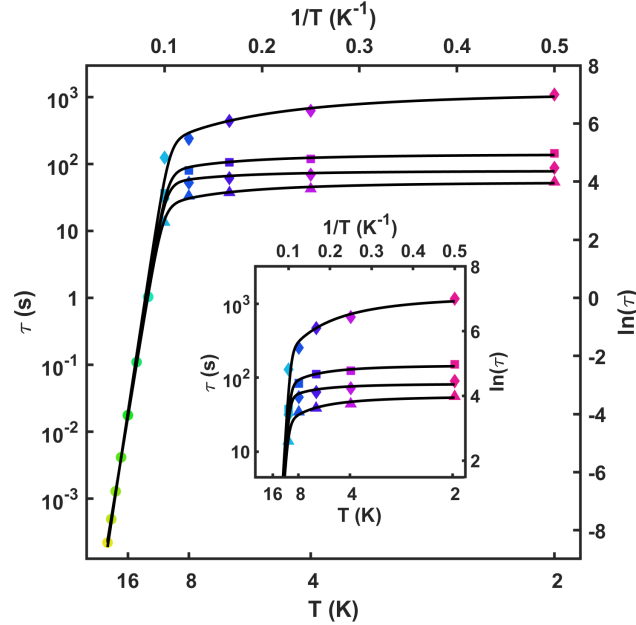


Figure 5: Standard AC relaxation times (circles), VSM waveform Debye fit (triangles), stretched exponential fit (squares), and bi-exponential fit (diamonds) of magnetic relaxation data for **1** with fit to relaxation model S1 (black line, parameters in Table S3). (Inset) Plot of τ vs. $1/T$ showing region of crossover between fitting methods. Black line again shows the relaxation model fit.

Susceptibility parameters extracted from Fourier analysis of the VSM waveform data (Figure 2) show a clear phase dependence on drive field frequency. In an approach analogous to that taken with standard AC susceptibilities, we fit in-phase and out-of-phase components of this data to a generalized Debye model (Equations 1 & 2, Table 1) and obtained α values close to 0 indicating that only a single characteristic relaxation time exists at each temperature. An Arrhenius plot of fitted relaxation times (Figure 5) shows that τ is weakly temperature dependent between 2–8 K and at 10 K τ begins to drop considerably as it approaches the high-temperature Orbach relaxation regime. We note that the relaxation time measured at 10 K via this method nearly matches the relaxation time predicted by an Arrhenius fit to the AC susceptibility data. This provides a strong indication that these methods are complementary probes of molecular magnetic relaxation for **1**. A comparison between relaxation times extracted from VSM waveforms and DC relaxation measurements reveal that each fitting method yields relaxation time profiles that deviate sublinearly from Arrhenius behavior. However, τ values obtained from exponential fits of DC data across the measured temperature range are consistently higher than the corresponding VSM waveform measurements. If we assume the Debye analysis to provide the most accurate τ , DC relaxation times extracted with Equation 3 (τ_{str}) and Equation 4 (τ_2) represent average errors of 270% and 175%, respectively. The long component of Equation 4, τ_1 represents an even more extreme error of 1261%.

Conclusions

In this work we have utilized the slow magnetic relaxation behavior of **1** to test the efficacy of a new technique for extracting characteristic relaxation times that are beyond the scope of standard AC susceptibility experiments. This proof-of-concept work has shown that the VSM waveform method is viable and yields results that are a consistent continuation of the fast timescale dynamics. We hope that given the wide availability of the required instrumentation and the current interest in understanding and controlling the rate of magnetic relaxation mechanisms access to another characterization tool will prove useful. In addition to the expanded timescale, the methods described herein may prove useful for targeting specific relaxation mechanisms that occur at non-zero field. For example, with the field tuned to a level-crossing, quantum-tunneling transitions could be studied in isolation from competing relaxation mechanisms.

Acknowledgements

This research was funded through the Office of Naval Research Young Investigator Award N00014-16-1-2917. The authors thank Drs. Milan Gembicky and Anthony L. Spek (crystallography) and Dr. Anthony Mrse (NMR) for their expert assistance.

References

- [1] Roberta Sessoli, Hui Lien Tsai, Ann R. Schake, Sheyi Wang, John B. Vincent, Kirsten Folting, Dante Gatteschi, George Christou, and David N. Hendrickson. High-spin molecules: $[\text{Mn}12\text{O}12(\text{O}2\text{CR})16(\text{H}2\text{O})4]$. *Journal of the American Chemical Society*, 115(5):1804–1816, March 1993.
- [2] R. Sessoli, D. Gatteschi, A. Caneschi, and M. A. Novak. Magnetic bistability in a metal-ion cluster. *Nature*, 365(6442):141–143, September 1993.
- [3] Markus Hiller, Martin Maier, Hubert Wadepohl, and Markus Enders. Paramagnetic NMR Analysis of Substituted Biscyclooctatetraene Lanthanide Complexes. *Organometallics*, 35(11):1916–1922, June 2016.
- [4] Paul A. Wender and Justin P. Christy. Nickel(0)-Catalyzed $[2 + 2 + 2 + 2]$ Cycloadditions of Terminal Dienes for the Synthesis of Substituted Cyclooctatetraenes. *Journal of the American Chemical Society*, 129(44):13402–13403, November 2007.
- [5] C. R. Groom, I. J. Bruno, M. P. Lightfoot, and S. C. Ward. The Cambridge Structural Database. *Acta Crystallographica Section B: Structural Science, Crystal Engineering and Materials*, 72(2):171–179, April 2016.
- [6] Katie R. Meihaus and Jeffrey R. Long. Magnetic Blocking at 10 K and a Dipolar-Mediated Avalanche in Salts of the Bis(*H*8-cyclooctatetraenide) Complex $[\text{Er}(\text{COT})2]^-$. *Journal of the American Chemical Society*, 135(47):17952–17957, November 2013.
- [7] Liviu Ungur, Jennifer J. Le Roy, Ilia Korobkov, Muralee Murugesu, and Liviu F. Chibotaru. Fine-tuning the Local Symmetry to Attain Record Blocking Temperature and Magnetic Remanence in a Single-Ion Magnet. *Angewandte Chemie*, 126(17):4502–4506, April 2014.
- [8] Jennifer J. Le Roy, Ilia Korobkov, and Muralee Murugesu. A sandwich complex with axial symmetry for harnessing the anisotropy in a prolate erbium(iii) ion. *Chemical Communications*, 50(13):1602–1604, 2014.
- [9] Jennifer J. Le Roy, Liviu Ungur, Ilia Korobkov, Liviu F. Chibotaru, and Muralee Murugesu. Coupling Strategies to Enhance Single-Molecule Magnet Properties of Erbium–Cyclooctatetraenyl Complexes. *Journal of the American Chemical Society*, 136(22):8003–8010, June 2014.
- [10] Shang-Da Jiang, Bing-Wu Wang, Hao-Ling Sun, Zhe-Ming Wang, and Song Gao. An Organometallic Single-Ion Magnet. *Journal of the American Chemical Society*, 133(13):4730–4733, April 2011.
- [11] Yin-Shan Meng, Chun-Hong Wang, Yi-Quan Zhang, Xue-Bing Leng, Bing-Wu Wang, Yao-Feng Chen, and Song Gao. (Boratabenzene)(cyclooctatetraenyl) lanthanide complexes: A new type of organometallic single-ion magnet. *Inorganic Chemistry Frontiers*, 3(6):828–835, June 2016.
- [12] J. D. Hilgar, B. S. Flores, and J. D. Rinehart. Ferromagnetic coupling in a chloride-bridged erbium single-molecule magnet. *Chemical Communications*, 53(53):7322–7324, June 2017.
- [13] J. D. Hilgar, M. G. Bernbeck, B. S. Flores, and J. D. Rinehart. Metal–ligand pair anisotropy in a series of mononuclear Er–COT complexes. *Chemical Science*, 9(36):7204–7209, September 2018.
- [14] Shi-Ming Chen, Jin Xiong, Yi-Quan Zhang, Qiong Yuan, Bing-Wu Wang, and Song Gao. A soft phosphorus atom to “harden” an erbium(III) single-ion magnet. *Chemical Science*, 9(38):7540–7545, October 2018.
- [15] Meng He, Xiao Chen, Tilmann Bodenstein, Andreas Nyvang, Sebastian F. M. Schmidt, Yan Peng, Eufemio Moreno-Pineda, Mario Ruben, Karin Fink, Michael T. Gamer, Annie K. Powell, and Peter W. Roesky. Enantiopure Benzamidinate/Cyclooctatetraene Complexes of the Rare-Earth Elements: Synthesis, Structure, and Magnetism. *Organometallics*, 37(21):3708–3717, November 2018.
- [16] Jeremy D. Hilgar, Maximilian G. Bernbeck, and Jeffrey D. Rinehart. Million-fold Relaxation Time Enhancement across a Series of Phosphino-Supported Erbium Single-Molecule Magnets. *Journal of the American Chemical Society*, 141(5):1913–1917, February 2019.
- [17] Liviu Ungur, Maarten Thewissen, Jean-Pierre Costes, Wolfgang Wernsdorfer, and Liviu F. Chibotaru. Interplay of Strongly Anisotropic Metal Ions in Magnetic Blocking of Complexes. *Inorganic Chemistry*, 52(11):6328–6337, June 2013.

- [18] Jun-Liang Liu, Yan-Cong Chen, and Ming-Liang Tong. Symmetry strategies for high performance lanthanide-based single-molecule magnets. *Chemical Society Reviews*, 47(7):2431–2453, April 2018.
- [19] Dante Gatteschi, Roberta Sessoli, and Jacques Villain. *Molecular Nanomagnets*. Oxford University Press, March 2006.

Supporting Information

Contents

1 Preparative Details	11
1.1 General Considerations	11
1.2 [K(18-c-6)][Er(hdcCOT) ₂] (1)	11
2 Sample Characterization	12
2.1 ¹ H NMR of K[Er(hdcCOT) ₂]	12
2.2 Crystallographic Methods	14
2.3 Computational Details	14
2.4 Magnetic Data Collection	16
References	21

1 Preparative Details

1.1 General Considerations

Manipulations involving the synthesis of **1** were carried out in a nitrogen-atmosphere glovebox. Tetrahydrofuran (THF) and pentane were dried on activated alumina columns and stored over a 1:1 mixture of 3 and 4 Å molecular sieves. 1,6-heptadiyne (purchased from Alfa Aesar) was degassed using freeze-pump-thaw cycles prior to use. Nickel(II) bromide DME complex (Combi-Blocks), 18-crown-6 (18-c-6, Aldrich), anhydrous erbium trichloride (Aldrich), and potassium graphite (KC₈, Strem) were used as received. THF-d₈ was purchased from Sigma-Aldrich and was degassed using freeze-pump-thaw cycles, dried over stage 0 NaK on silica, and filtered before use. Neutral proligand hdcCOT was synthesized according to a literature procedure.¹ ¹H NMR spectra were collected at -20 °C on a Jeol ECA 500 spectrometer. CHN elemental analysis was conducted by Midwest Microlab, Indianapolis, IN.

1.2 [K(18-c-6)][Er(hdcCOT)₂] (**1**)

To a -50 °C stirring suspension of KC₈ (0.368 g, 2.72 mmol, 4 mL THF) was added a solution of hdcCOT (0.239 g, 1.30 mmol, 6 mL THF). The reaction mixture was allowed to warm to room temperature and was stirred for a total of 16 hours. Graphite was removed *via* centrifugation and subsequent filtration through a glass-fiber filter yielded a dark brown homogeneous solution. Concentration *in vacuo* and cooling to -50 °C yielded large yellow plates of K₂hdcCOT over the course of 24 hours. The mother liquor was removed from these plates and they were subsequently dried *in vacuo*; mass obtained: 0.261 g (Yield: 76.5%). K₂hdcCOT (0.182 g, 0.693 mmol) and ErCl₃ (0.095 g, 0.347 mmol) were combined in 20 mL THF and stirred for 16 hours. The resulting yellow suspension was centrifuged and the supernatant was separated and dried *in vacuo* to yield 0.149 g (74.7%) of K[Er(hdcCOT)₂] as a bright yellow powder. 18-crown-6 (0.0635 g, 0.240 mmol) was combined with this powder (0.1382 g, 0.240 mmol) in 20 mL THF and the resulting solution was stirred for 16 hours. Vapor diffusion of pentane into this solution yielded yellow rods of **1** (200 mg, Yield: 85.0%). CHN analysis (calculated, found) for C₄₀H₅₆ErK: C (57.25, 54.26); H (6.73, 6.51); N (0, 0).

2 Sample Characterization

2.1 ^1H NMR of $\text{K}[\text{Er}(\text{hdcCOT})_2]$

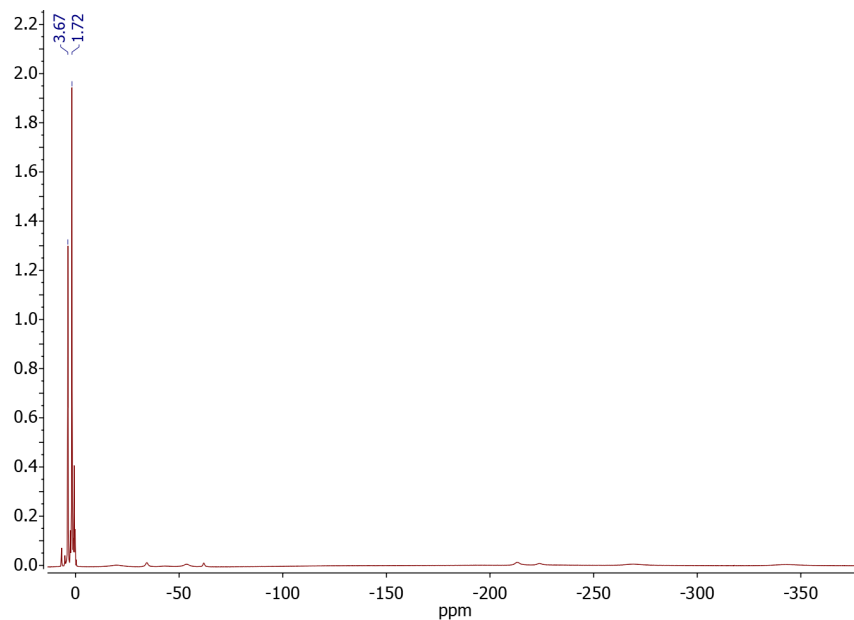


Figure S1: ^1H NMR spectrum of $\text{K}[\text{Er}(\text{hdcCOT})_2]$ in THF-d_8 at $-20\text{ }^\circ\text{C}$. Labelled signals correspond to THF residual peaks.

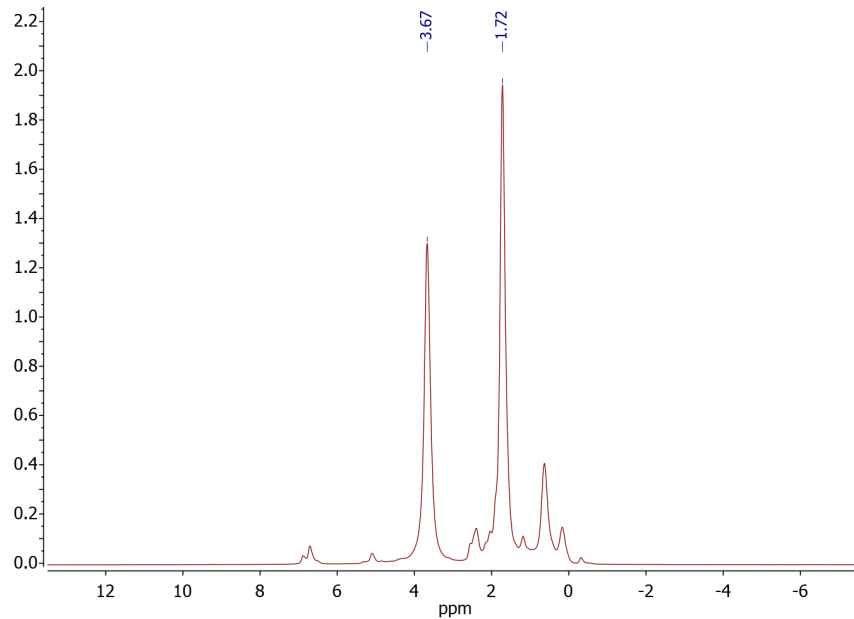


Figure S2: Downfield ^1H NMR spectrum of $\text{K}[\text{Er}(\text{hdcCOT})_2]$ in THF-d_8 at $-20\text{ }^\circ\text{C}$. Labelled signals correspond to THF residual peaks. Unlabelled signals are taken to be decomposition products.

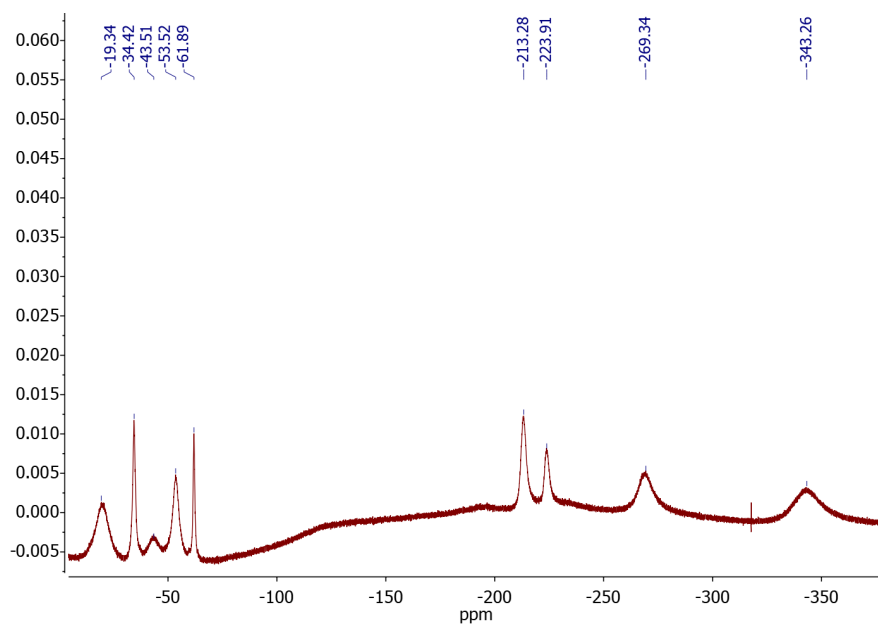


Figure S3: Upfield ^1H NMR spectrum of $\text{K}[\text{Er}(\text{hdcCOT})_2]$ in THF-d_8 at $-20\text{ }^\circ\text{C}$. Labelled signals correspond hdcCOT protons.

2.2 Crystallographic Methods

Single crystal diffraction data for **1** was collected at 100 K on a Bruker κ Diffractometer using a Ga(K_α) METALJET source and a PHOTON II Area Detector. Data integration was carried out using SAINT and output intensities were corrected for Lorentz and air absorption effects. Additional absorption corrections were applied using SADABS. The structure was solved in space group No. 14 ($P2_1/n$) using direct methods with the SHELXT² program and anisotropic atom positions were refined against F^2 data using the SHELXL³ program. Olex² was used during the refinement stage as a graphical front-end.⁴ Real and imaginary anomalous dispersion coefficients for Ga(K_α) radiation were taken from the Brennan and Cowan⁵ model. The position of all hydrogen atoms were determined using a riding model. Supplementary crystallographic data can be accessed from the Cambridge Crystallographic Data Center, CCDC 1939762.

2.3 Computational Details

Ab initio electronic structure modelling was carried out at the CASSCF level using the MOLCAS 8.2 software suite. Input atom coordinates were taken from crystallographic data and used without further geometry optimization. K, 18-c-6, and solvent THF were excluded from the input geometry. Basis functions of the ANO-RCC type were generated with the SEWARD module and the quality of a specific atomic basis function was determined as a function of the atom's distance from the Er³⁺ ion (**Er**: ANO-RCC-VTZP; **atoms bound to Er**: ANO-RCC-VDZP; **all other atoms**: ANO-RCC-VDZ). To save disk space and reduce calculation cost two-electron integrals were Cholesky decomposed (10^{-6} cutoff). A 7-orbital, 11-electron activate space (CAS(11,7)) was selected for the CASSCF calculation which was carried out with the RASSCF module. In this space all 35 configuration-interaction (CI) roots of spin multiplicity 4 and all 112 CI roots of spin multiplicity 2 were included. Spin-orbit matrix elements between CAS output wavefunctions were calculated with the RASSI module. SINGLE_ANISO was used to calculate relevant magnetic properties based on these multiconfigurational SCF results.

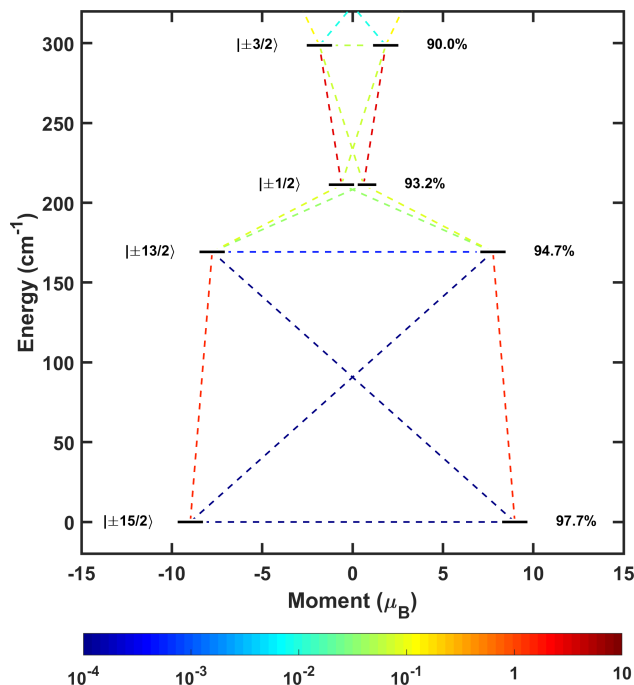


Figure S4: Calculated spectrum of the four lowest energy Kramers states for **1**. States (black lines) are labelled by their largest $\pm m_J$ component (left) and the percentage of that component (right). Transverse magnetic moment matrix elements (dotted lines) are colored according to their respective values (colorbar).

Table S1: $J = 15/2$ manifold energy spectrum of **1**.

KD (i)	$M_z (\mu_B)$	$E (\text{cm}^{-1})$
G	8.976951952	0.000
1	7.769140677	169.229
2	0.613462182	211.322
3	1.834519491	298.637
4	6.547320548	411.560
5	3.031744486	433.319
6	4.722208148	542.787
7	5.730749227	550.231

Table S2: Selected average magnetic moment matrix elements between the $J = 15/2$ multiplets of **1**.

KD (i)	$\langle i_{\uparrow} \hat{M}_{avg} i_{\downarrow} \rangle$	$\langle i_{\uparrow} \hat{M}_{avg} i_{\uparrow} + 1 \rangle$	$\langle i_{\uparrow} \hat{M}_{avg} i_{\downarrow} + 1 \rangle$
G	0.327451096777E-05	0.155011707285E+01	0.131694298009E-04
1	0.506016013299E-03	0.928060135350E-01	0.405995456082E-01
2	0.318682266522E+01	0.316661251988E+01	0.720938920092E-01
3	0.600396549586E-01	0.134946515237E+00	0.941722228670E-02
4	0.142404299502E-02	0.242852634761E+00	0.973779023853E-02
5	0.485270066726E-01	0.285000005858E+01	0.300470628704E-01
6	0.549287282880E-01	0.266558195629E+01	0.429984200984E-01
7	0.508798096471E-01		

2.4 Magnetic Data Collection

Magnetic data were collected under DC scan and VSM scan modes using a Quantum Design MPMS 3 SQUID Magnetometer with equipped AC susceptibility attachment. Samples were loaded in custom quartz tubes (D&G Glassblowing Inc.) which were subsequently flame-sealed under static vacuum. To all samples was added a portion of melted eicosane wax to abate sample torquing and facilitate thermal conductivity. Diamagnetic contributions from the sample and eicosane were subtracted from all static moment data using Pascal's constants.⁶ Magnetic relaxation data were collected in DC scan mode after first equilibrating the sample at a given temperature to a 7 T field then ramping the field (700 Oe sec^{-1}) to 0 T. Details related to the Fourier analysis of long-timescale magnetic data are discussed in the main text. MPMS3 data parsing, fitting, and plotting was performed with MATLAB; the object-oriented code package and documentation used for all processes is available at <https://www.github.com/RinehartGroup/qdsquid-dataplot>.

$$\tau^{-1} = \tau_0^{-1} \exp\left(\frac{-U_{eff}}{k_B T}\right) + \tau_{qtm}^{-1} + CT^2 \quad (\text{S1})$$

Relaxation mechanism equation

Listing 1: Truncated MPMS3 MultiVu Sequence

```
1 Set Temperature 50K at 50K/min, Fast Settle
2 Wait For Temperature, Delay 0 sec, No Action
3
4 Magnet Reset
5 Wait For Delay 600 secs (10.0 mins), No Action
6
7 Set Temperature 2K at 50K/min. Fast Settle
8 Wait For Temperature, Delay 120 secs (2.0 mins), No Action
9
10 ! REMARK - Frequency ~ 0.0264 Hz
11 MPMS3 Measure for 0.5 sec at 1 mm every 0 sec Auto-Tracking
12 Wait For Delay 2 secs, No Action
13 Scan Time 0.0 secs in 20 steps
14     Set Magnetic Field 8.00e at 30.000e/sec, Linear, Stable
15     Wait For Field, Delay 15 secs, No Action
16     Set Magnetic Field -8.00e at 30.000e/sec, Linear, Stable
17     Wait For Field, Delay 15 secs, No Action
18 End Scan
19 Set Magnetic Field 0.00e at 30.000e/sec, Linear, Stable
20 Wait For Field, Delay 0 secs, No Action
21 Stop Measurements
22
23 Wait For Delay 60 secs (1.0 mins), No Action
24
25 ! REMARK - Frequency ~ 0.0147 Hz
26 MPMS3 Measure for 0.5 sec at 1 mm every 0 sec Auto-Tracking
27 Wait For Delay 2 secs, No Action
28 Scan Time 0.0 secs in 16 steps
29     Set Magnetic Field 8.00e at 30.000e/sec, Linear, Stable
30     Wait For Field, Delay 22 secs, No Action
31     Set Magnetic Field -8.00e at 30.000e/sec, Linear, Stable
32     Wait For Field, Delay 22 secs, No Action
33 End Scan
34 Set Magnetic Field 0.00e at 30.000e/sec, Linear, Stable
35 Wait For Field, Delay 0 secs, No Action
36 Stop Measurements
37
38 ! REMARK - Frequencies truncated
39
40 Wait For Delay 240 secs (4.0 mins), No Action
41
42 ! REMARK - Frequency ~ 0.00013 Hz
43 MPMS3 Measure for 0.5 sec at 1 mm every 0 sec Auto-Tracking
44 Wait For Delay 2 secs, No Action
45 Set Magnetic Field 8.00e at 30.000e/sec, Linear, Stable
46 Wait For Field, Delay 3840 secs (1.1 hours), No Action
47 Set Magnetic Field -8.00e at 30.000e/sec, Linear, Stable
48 Wait For Field, Delay 3840 secs (1.1 hours), No Action
49 Set Magnetic Field 0.00e at 30.000e/sec, Linear, Stable
50 Wait For Field, Delay 0 secs, No Action
51 Stop Measurements
52
53 Set Temperature 300K at 50K/min. Fast Settle
54 Wait For Temperature, Delay 1 secs, No Action
```

Table S3: Fitting values for relaxation mechanism parameters. Note these parameters are meant to highlight differences in the form of the relaxation data determined by different methods and are purely phenomenological.

	U_{eff} (cm ⁻¹)	τ_0 (s)	τ_{qtm} (s)	C (K ⁻² s ⁻¹)
τ_{AC}	147.7(7)	$3.1(1) \times 10^{-8}$		
$\tau_{AC} + \tau_{VSM}$	142(3)	$4.7(1.0) \times 10^{-8}$	54(7)	$2.2(8) \times 10^{-4}$
$\tau_{AC} + \tau_{str}$	146(5)	$3.5(1.1) \times 10^{-8}$	141(31)	$6.2(6.2) \times 10^{-5}$
$\tau_{AC} + \tau_1$	154(13)	$1.8(1.0) \times 10^{-8}$	1209(621)	$4.0(4.2) \times 10^{-5}$
$\tau_{AC} + \tau_2$	145(6)	$3.6(1.2) \times 10^{-8}$	80(17)	$6.9(9.7) \times 10^{-5}$

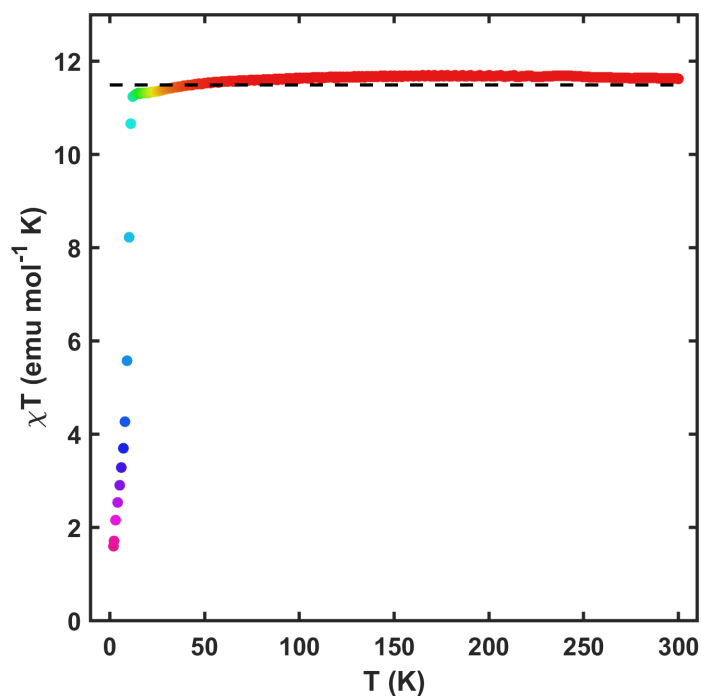


Figure S5: Magnetic susceptibility of **1** between 2 to 300 K. Colored dots are data measured under a 1000 Oe field and the dotted line is the theoretical χT value for a free Er³⁺ ion.

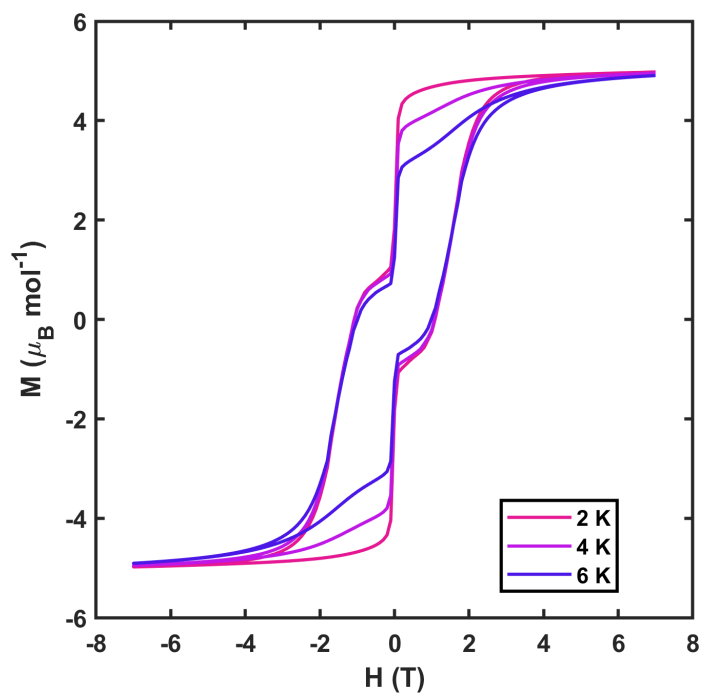


Figure S6: Isothermal magnetization of **1** from -7 to 7 T (Rate = 10 Oe sec^{-1}).

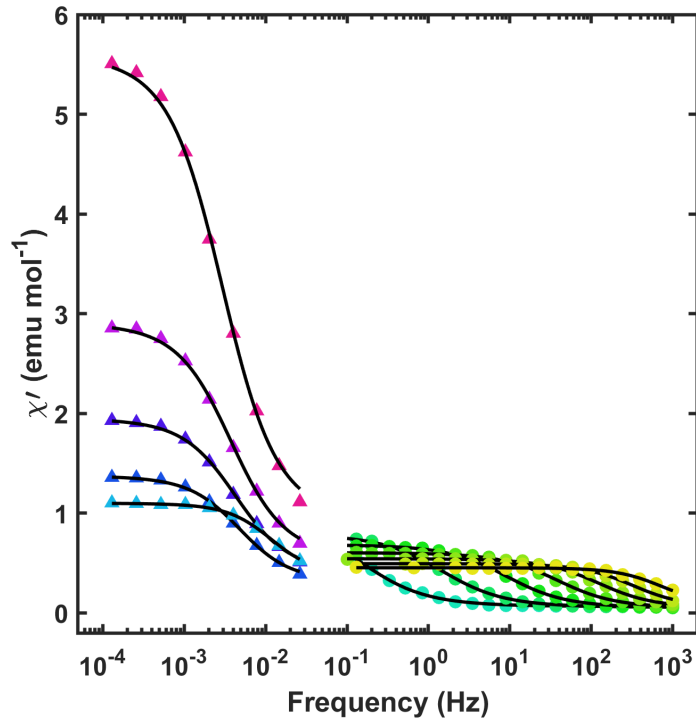


Figure S7: In-phase magnetic susceptibility of **1** between 2 (fuschia) and 24 (yellow) K. Colored points are susceptibilities measured via standard AC measurements (circles) and extracted from Fourier analysis of VSM data (triangles). Black lines represent fits to a generalized Debye model (Equations 1 & 2).

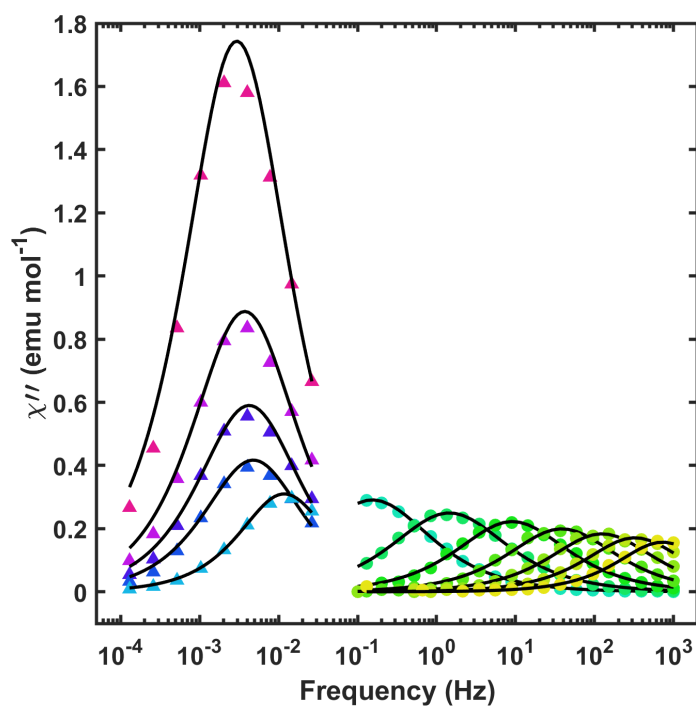


Figure S8: Out-of-phase magnetic susceptibility of **1** between 2 (fuschia) and 24 (yellow) K. Colored points are susceptibilities measured via standard AC measurements (circles) and extracted from Fourier analysis of VSM data (triangles). Black lines represent fits to a generalized Debye model (Equations 1 & 2).

References

- [1] Paul A. Wender and Justin P. Christy. Nickel(0)-Catalyzed [2 + 2 + 2 + 2] Cycloadditions of Terminal Diynes for the Synthesis of Substituted Cyclooctatetraenes. *Journal of the American Chemical Society*, 129(44):13402–13403, November 2007.
- [2] G. M. Sheldrick. SHELXT – Integrated space-group and crystal-structure determination. *Acta Crystallographica Section A: Foundations and Advances*, 71(1):3–8, January 2015.
- [3] G. M. Sheldrick. Crystal structure refinement with SHELXL. *Acta Crystallographica Section C: Structural Chemistry*, 71(1):3–8, January 2015.
- [4] O. V. Dolomanov, L. J. Bourhis, R. J. Gildea, J. a. K. Howard, and H. Puschmann. OLEX2: a complete structure solution, refinement and analysis program. *Journal of Applied Crystallography*, 42(2):339–341, April 2009.
- [5] S. Brennan and P. L. Cowan. A suite of programs for calculating x-ray absorption, reflection, and diffraction performance for a variety of materials at arbitrary wavelengths. *Review of Scientific Instruments*, 63(1):850–853, January 1992.
- [6] Gordon A. Bain and John F. Berry. Diamagnetic Corrections and Pascal’s Constants. *Journal of Chemical Education*, 85(4):532, April 2008.